Numerical Simulations of an Advection Fog Event over Shanghai Pudong International Airport with the WRF Model

Caiyan LIN[1*], Zhongfeng ZHANG[1], Zhaoxia PU[2], and Fengyun WANG[3]

1 *Aviation Meteorological Center*, *Air Traffic Management Bureau*, *Civil Aviation Administration of China*, *Beijing* 100122, *China*
2 *Department of Atmospheric Sciences*, *University of Utah*, *UT* 84112, *USA*
3 *Meteorological Center*, *East China Air Traffic Management Bureau*, *Civil Aviation Administration of China*, *Shanghai* 200335, *China*

(Received November 20, 2016; in final form July 11, 2017)

ABSTRACT

A series of numerical simulations is conducted to understand the formation, evolution, and dissipation of an advection fog event over Shanghai Pudong International Airport (ZSPD) with the Weather Research and Forecasting (WRF) model. Using the current operational settings at the Meteorological Center of East China Air Traffic Management Bureau, the WRF model successfully predicts the fog event at ZSPD. Additional numerical experiments are performed to examine the physical processes associated with the fog event. The results indicate that prediction of this particular fog event is sensitive to microphysical schemes for the time of fog dissipation but not for the time of fog onset. The simulated timing of the arrival and dissipation of the fog, as well as the cloud distribution, is substantially sensitive to the planetary boundary layer and radiation (both longwave and shortwave) processes. Moreover, varying forecast lead times also produces different simulation results for the fog event regarding its onset and duration, suggesting a trade-off between more accurate initial conditions and a proper forecast lead time that allows model physical processes to spin up adequately during the fog simulation. The overall outcomes from this study imply that the complexity of physical processes and their interactions within the WRF model during fog evolution and dissipation is a key area of future research.

Key words: advection fog, physical parameterization, numerical prediction, forecast lead time, WRF model

Citation: Lin, C. Y., Z. F. Zhang, Z. X. Pu, et al., 2017: Numerical simulations of an advection fog event over Shanghai Pudong International Airport with the WRF model. *J. Meteor. Res.*, **31**(5), 874–889, doi: 10.1007/s13351-017-6187-2.

1. Introduction

Fog is a weather phenomenon caused by the suspension of tiny liquid water droplets or ice crystals in the air at or near the earth's surface, during which horizontal visibility is less than 1 km. The adverse effects of fog on human activities, especially on aviation, marine, and land transportation, are well known (e.g., Bergot et al., 2007; Fabbian et al., 2007; Gultepe et al., 2007, 2015; Fu et al., 2010; Niu et al., 2010; Stolaki et al., 2012). A common type of fog that often influences coastal regions is advection fog, which forms when quite warm, moist air is blown across a cooler surface. For instance, over the east coast of China, Shanghai Pudong International Airport (ZSPD) is a major aviation hub for Asia, where the air traffic is frequently disturbed by advection fog from the East China Sea (ECS) in winter and spring (Yuan and Chen, 2013). Accurate prediction of advection fog at ZSPD and in its vicinity is becoming more and more important for providing better aviation service and reducing delays and economic loss.

Significant progress has been made in fog prediction and visibility parameterization with the development of several fog prediction models (e.g., Bergot and Guedalia, 1994; Clark and Hopwood, 2001a, b; Bott and Trautmann, 2002), visibility algorithms (Doran et al., 1999; Stoelinga and Warner, 1999; Bieringer et al., 2006; Gultepe et al., 2006, 2009; Bang et al., 2009; Gultepe and Milbrandt, 2010; Creighton et al., 2014), and improved numerical weather prediction (NWP) models for fog pre-

Supported by the National Natural Science Foundation of China (4130511 and U1233138) and Safety Capability Enhancement Program of Civil Aviation Administration of China (TMSA1605).

*Corresponding author: lincaiyan@atmb.net.cn.

diction and simulations (e.g., Fu et al., 2010; Kim and Yum, 2012; Román-Cascón et al., 2012, 2016; Hu et al., 2014; Payra and Mohan, 2014). Several factors that influence fog prediction, such as the initial conditions (Rémy et al., 2012; Bari et al., 2015), model resolution (Tardif, 2007; Tang et al., 2009; Van der Velde et al., 2010), terrain (Golding, 1993), turbulence (Li and Zheng, 2015), and vegetation (von Glasow and Bott, 1999), have been investigated by using NWP models.

In particular, the Weather Research and Forecasting (WRF) model (Skamarock et al., 2008), which allows the use of different combinations of physical parameterizations and technical configurations, has been used to investigate the sensitivity of model attributes in fog simulations. For instance, Radi et al. (2008) found that the combination of the Lin microphysical scheme (Lin et al., 1983), Yonsei University (YSU) planetary boundary layer (PBL) scheme (Hong et al., 2006), Noah land surface model (LSM), RRTM longwave radiation (Mlawer et al., 1997), and Dudhia shortwave radiation (Dudhia, 1989), was the best for their modeling of thick coastal fog along the west coast of the United Arab Emirates (UAE) with the WRF model. They also found that coastal fog occurrence in the UAE was well predicted with a forecast lead time of 24 h or more when they used the Global Forecast System (GFS) analyses as initial states. This is similar to the results of Román-Cascón et al. (2016), who reported that simulations with a forecast lead time of 30 h are usually better than those with only 6 h of spin-up, based on their radiation fog cases in Spain and the Netherlands. Van der Velde et al. (2010) evaluated the sensitivity of simulation of a severe radiation fog over the Netherlands to microphysics (Kessler, Eta Ferrier, WRF single-moment WSM3, WSM5, and WSM6); to PBL [YSU and Mellor–Yamada–Janjić (MYJ)]; and to land surface (five-layer thermal diffusion and Noah LSM) schemes, and showed a failure to correctly simulate the fog with any of the parameterizations of WRF and a relatively better performance with WSM3/YSU/Noah LSM. Román-Cascón et al. (2012) compared the skill of different PBL and land surface schemes, and options for the gravitational settling of cloud/fog droplets in the WRF model for three radiation fog events at the Spanish Northern Plateau and indicated that the results were case dependent. Steeneveld et al. (2015) found that the impacts of microphysics and PBL parameterizations on the simulation of two radiation fog episodes over the Netherlands were different over different areas, and the onset of modeled fog depended more on PBL while the dispersal was more sensitive to the microphysics schemes.

Overall, previous studies show that the sensitivity of numerical simulations of fog to physical options and configurations in NWP models is somewhat case and location dependent, especially for the physical parameterizations. For advection/coastal fog, several studies have also been conducted to investigate the sensitivity of NWP models on fog simulation, such as the initial conditions and the physical parameterizations (e.g., Pagowski et al., 2004; Nakanishi and Niino, 2006; Radi et al., 2008; Zhou, 2011; Kim and Yum, 2012; Hu et al., 2014; Li and Zheng, 2015). However, to the best of our knowledge, there is not a comprehensive study that examines the sensitivity of the numerical prediction of advection fog to the physical parameterization schemes in the WRF model. Therefore, it is still not clear whether the prediction of advection fog is strongly influenced by the various physical processes in the models, especially in a particular region such as ZSPD. In addition, despite all the previous research on fog simulations, fog is still a forecasting challenge for NWP models (Van der Velde et al., 2010; Román-Cascón et al., 2012, 2016; Zhou et al., 2012; Steeneveld et al., 2015).

Recently, the WRF model has been adopted for operational forecasting at the Meteorological Center of East China Air Traffic Management Bureau (ATMB), which makes it possible to forecast advection fog with a numerical model and to also conduct sensitivity studies for understanding the sensitivity of simulations and forecasts of advection fog to different physical parameterization schemes, especially the onset and dispersal timing of fog events. Therefore, in this study, we aim at these goals by evaluating the sensitivity of numerical simulations of an advection fog event to WRF physical parameterizations around the ZSPD region. Our intention is to understand what the important physical processes and factors are associated with the accurate prediction of advection fog. A typical advection fog event that occurred in the rear part of a high-pressure system that moved eastwards to the ECS during 26–27 March 2014 is examined in this study. The sensitivity of the forecasting results to forecast lead times is also examined.

The paper is organized as follows. An overview of the fog event and its synoptic background are briefly given in Section 2, followed by a description of the control simulation, validation, and visibility algorithms in Section 3. Section 4 describes the sensitivity experiments and corresponding results. Finally, summary and concluding remarks are presented in Section 5.

2. Case description

During 26–27 March 2014, a fog event was observed

over the western ECS that invaded ZSPD and persisted for about 6 h. According to the Meteorological Aviation Report (METAR) at ZSPD, a sudden decrease in visibility and appearance of a low ceiling occurred on 26 March 2014. This transition took place as the wind shifted from northeasterly to easterly and then southeasterly with a speed around 3 m s^{-1}. A sudden appearance of a cloud ceiling below 100 m was observed at 1700 UTC, followed by the fog onset as a "wall" of fog reached ZSPD at 1930 UTC, with an associated sudden jump in visibility (dropping sharply from 2 to 0.2 km within 0.5 h). According to the fog classification applied in Tardif and Rasmussen (2007), these conditions are indicative of a fog layer being advected inland from the coastal ocean, and thus this event is categorized as an advection fog.

Figure 1 shows snapshots of the synoptic situation from the NCEP global final analysis (FNL) and surface synoptic observations (SYNOP). The FNL analysis shows that the ECS and its west coast were controlled by a wide trough tilted northeast to southwest at 500 hPa, which moved slowly eastwards from 0600 UTC 26 to 0000 UTC 27 March (figures omitted). At the lower levels, there was a transition from domination by a low-pressure system at 0600 UTC 26 March to that by a high-pressure system (e.g., Fig. 1c shows the surface condition at 1800 UTC 26 March). The moist air concentrated mainly at the lower levels and moved westwards after 1200 UTC 26 March (figures omitted), and horizontal winds veered from northwest/north–northeast to east–northeast at about 1800 UTC 26 March before the fog was advected to ZSPD (Fig. 2). There was also an obvious temperature inversion layer that developed aloft from 1200 UTC 26 to 0000 UTC 27 March, with the inversion top at about 1000 m above ground level, which provided the stable weather conditions for fog/clouds to develop and maintain at the lower levels (Fig. 2). The temperature at the near-surface levels was warmer than the sea surface temperature (SST; red numbers in the bottom of Figs. 2d–f).

At 1800 UTC 26 March, the SST field showed a trough over the western ECS (Fig. 2c), the 2-m air temperature was warmer than the SST (figures omitted), and some warm moist air was moving westwards with a speed of 4 m s^{-1} (weak warm advection; Figs. 2c, e). The horizontal temperature advection, as shown from the longitude–height section across ZSPD, revealed a cold ad-

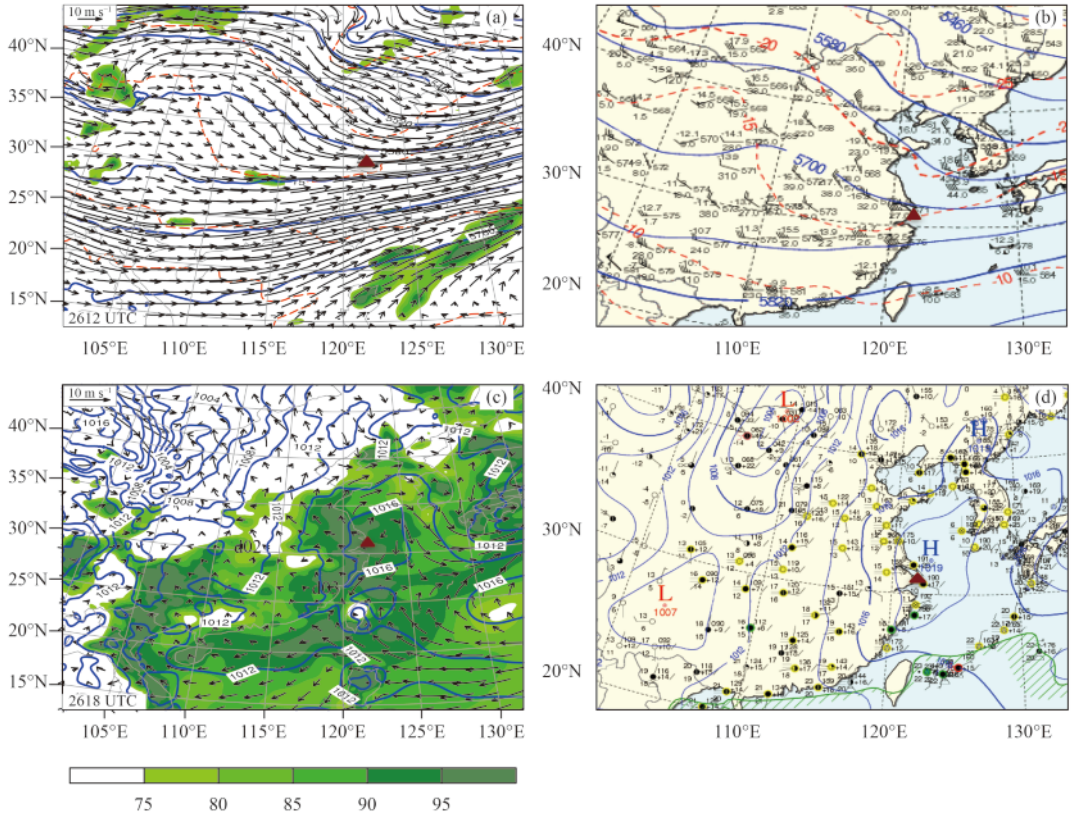

Fig. 1. Synoptic conditions from (a, c) NCEP FNL analysis and (b, d) surface synoptic observations (SYNOP), (a, b) at 500 hPa at 1200 UTC 26 March and (c, d) at the surface at 1800 UTC 26 March. The blue lines represent geopotential height in (a, b) and sea level pressure in (c, d). The green shaded area in (a, c) denotes relative humidity greater than 75%. The red triangle denotes the location of ZSPD (Shanghai Pudong International Airport).

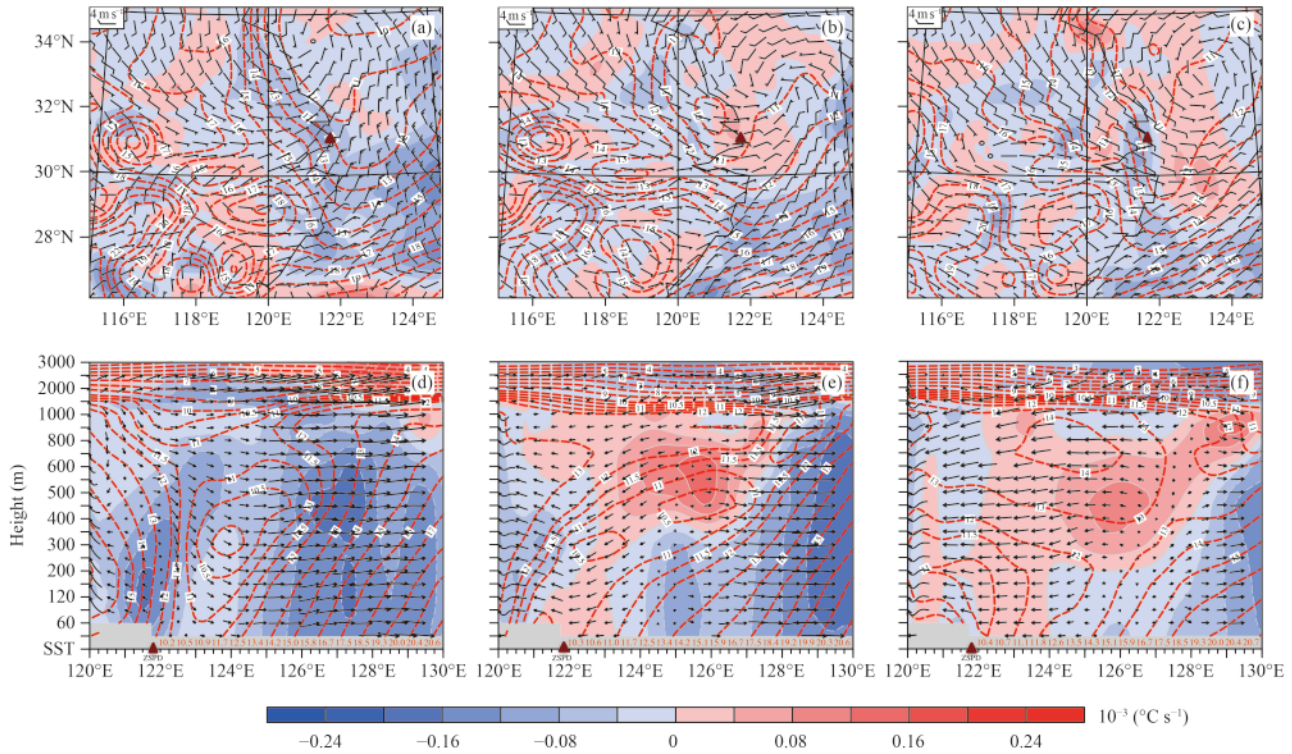

Fig. 2. (a–c) Horizontal distributions of air temperature (red dashed line), temperature advection at 2 m (shading), and horizontal winds at 10 m at (a) 1200 UTC 26, (b) 1800 UTC 26, and (c) 0000 UTC 27 March 2014. (d–f) Longitude–height sections across ZSPD of air temperature (red dashed line), temperature advection (shading), zonal–vertical winds (where vertical winds were multiplied by 1000), and SST (red numbers at the bottom) at (d) 1200 UTC 26, (e) 1800 UTC 26, and (f) 0000 UTC 27 March 2014. The red triangle denotes the location of ZSPD.

vection at 1200 UTC 26 March and then a warm advection layer over the ZSPD and ECS at 1800 UTC 26 March. At 0000 UTC 27 March, warm advection began to move eastwards from the coast.

Observations from the Vaisala LAP-3000 Lower Atmosphere Wind Profiler at ZSPD showed that winds started to veer from northerly to northeasterly below about 500 m after around 1100 UTC 26 March, and turned east–northeasterly at about 1600 UTC and then southeasterly at about 1900 UTC (red wind barbs in Fig. 3). The veering of the winds gradually extended up to the higher levels. The speed of the southeasterly wind increased up to 6 m s^{-1} after 0130 UTC 27 March.

The stable stratification and warm moisture advection over the cooler surface provided favorable conditions for fog formation and its subsequent advection to the west coast. In addition, the variation of the winds reasonably demonstrates the timing of fog onset and dispersal at ZSPD.

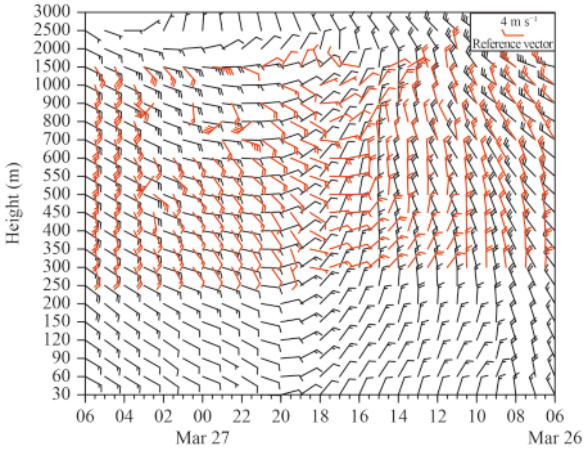

Fig. 3. Temporal evolution of vertical distributions of wind from a WRF 24-h simulation (black) and wind profiler observations (red) at ZSPD from 0600 UTC 26 to 0600 UTC 27 March 2014.

3. Control simulation and validation

3.1 *Model set-up*

The model used in this study is the Advanced Research version of the WRF model (Skamarock et al., 2008), version 3.6.1, which was released in August 2014. A two-way, three-level nested domain technique is used. The model settings follow the operational settings of the Meteorological Center of East China ATMB. The domains are defined in a Lambert conformation (see Fig. 4) with the center at (31°N, 120°E), and 41 vertical levels

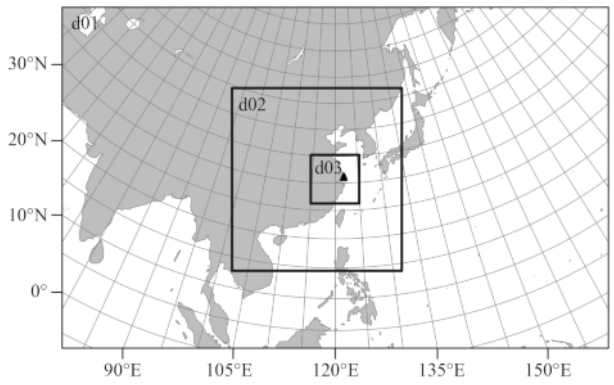

Fig. 4. Locations of the model domains. The triangle denotes ZSPD (Shanghai Pudong International Airport).

are used, with the model top at 50 hPa. As shown in Fig. 4, the horizontal resolutions are set at 36 km (d01; 313 × 195 points), 12 km (d02; 292 × 313 points), and 4 km (d03; 250 × 250 points), for the three nested domains, respectively. Initial and boundary conditions are derived from the NCEP Global Forecast System (GFS) final analysis (FNL) on 1° × 1° grids, available every 6 h. All model results in this paper are based on the forecasts from the innermost domain (d03), except for the analysis of the synoptic situations.

The physical parameterization schemes (Table 1) include the Thompson microphysical scheme (Thompson et al., 2008), YSU PBL scheme (Hong et al., 2006), RRTMG longwave radiation (RALW) scheme (Iacono et al., 2008), Dudhia shortwave radiation (RASW) scheme (Dudhia, 1989), Kain cumulus parameterization scheme (Kain, 2004; used only in d01 and d02), a revised MM5 Monin–Obukhov surface layer, and the unified Noah LSM (Chen and Dudhia, 2001). This configuration was identified as the baseline of an optimal combination from the operational forecasting in the ATMB of East China, specifically for the Shanghai area in general, although not only for fog forecasting. A control simulation initialized at 0600 UTC 26 March 2014 is selected for better simulation of the fog duration, the reason of which will be subsequently investigated.

3.2 *Validation of the control simulation*

Good agreement is found between the simulations (figures omitted) and the FNL analysis and SYNOP observations (as illustrated in Fig. 1). The control simulation well predicts the key features of the synoptic conditions. The simulated geopotential height and temperature at 925, 850, 700, and 500 hPa at 1200 and 1800 UTC 26 March and 0000 UTC 27 March also agree well with the corresponding FNL analysis (figures omitted).

The simulated vertical profiles of horizontal winds are further compared with the wind observations from the Vaisala LAP-3000 Lower Atmosphere Wind Profiler at ZSPD from 300 to 3000 m (Fig. 3). In the simulation, the veering of winds below 500 m from northwesterly–northerly to northeasterly–easterly occurs a bit later and persists much longer than in the observations, resulting in a later fog onset (around 0.5–1 h later) and dissipation (around 1–1.5 h later) at ZSPD when compared with observations, even for the results based on most of the visibility algorithms. Although there are some discrepancies between the simulated and observed winds, they overall agree well in many aspects.

In order to predict fog and also to evaluate the performance of the WRF model, selection of an effective visibility algorithm is necessary. To identify a proper method that can represent advection fog at ZSPD, the performance of eight algorithms is first evaluated and compared. These algorithms include SW99 (Stoelinga and Warner, 1999); the US National Oceanic and Atmospheric Administration Forecast Systems Laboratory (FSL) method (Doran et al., 1999); an algorithm called CVIS that combines the SW99 and FSL methods (Bang et al., 2009); the US Air Force Weather Agency (AFWA) diagnostic method in WRF (Creighton et al., 2014); the two algorithms used in NCEP's Unified Post Processor version 2.2 (called UPP1 and GSD); and those in Gultepe et al. (2006; called G2006) and Gultepe et al. (2009, called G2009). Detailed descriptions of the algorithms are provided in Table 2.

Among these algorithms, SW99, UPP1, G2006, and G2009 consider only the effect of light extinction from hydrometeors, while FSL calculates the visibility based on relative humidity (RH) and CVIS takes the minimum between the SW99 and FSL algorithms. The AFWA algorithm includes the effect of hydrometeors (rain, graupel, and snow), dust, and RH on surface visibility, but does not account for the contribution of cloud water and cloud ice in considering the poor model performance in cloud water and cloud ice predictions near the surface. The GSD algorithm integrates almost all the possible factors included in other algorithms.

Table 1. Physical parameterization schemes used in the control simulation

Microphysics	PBL	Surface layer	Longwave radiation	Shortwave radiation	Cumulus convection	Land surface
Thompson	YSU	Revised MM5 Monin–Obukhov	RRTMG	Dudhia	Kain	Unified Noah land-surface model

As shown in Fig. 5, with most of these visibility algorithms, the model successfully predicts the fog event, with consistent timing of the onset and dissipation of fog. Except for AFWA, all algorithms can capture the fog event (defined as visibility less than 1 km), although almost all schemes underestimate the visibility during the fog's lifetime, with some showing a slightly earlier onset and some a later dispersal. Since the AFWA algorithm estimates the surface visibility due to fog or haze based on RH without considering cloud water, it is inadequate in this case as cloud water near the surface is not counted. For those algorithms that consider only the effect of light extinction from hydrometeors (e.g., SW99, UPP1, G2006, and G2009), visibility varies sharply from very high (more than tens of kilometers) to very low; of these, G2009 does not underestimate the visibility as much as the other algorithms.

Because the GSD algorithm is more complicated and compatible with other algorithms, we choose the GSD in this case to calculate the visibility for the rest of the sensitivity experiments reported in the following section.

4. Sensitivity experiments and results

As mentioned in the introduction, it is of great interest to examine whether the forecasting of advection fog is sensitive to various forecast lead times and physical parameterization schemes. Therefore, additional sensitivity experiments are performed. For the sensitivity experiments for each type of physical parameter, only those schemes that have been heavily tested, i.e., those that are considered as candidates for updating operational sys-

Table 2. Descriptions of the visibility algorithms

Abbreviation	Visibility algorithm (VIS; unit: km)	Reference
SW99	$\mathrm{VIS_{SW99}} = -\ln(0.02)/\beta$, $\beta = \beta_{cw} + \beta_{rw} + \beta_{ci} + \beta_{sn}$. $\beta_{cw} = 144.7{C_{cw}}^{0.88}$, $\beta_{rw} = 1.1{C_{rw}}^{0.75}$, $\beta_{ci} = 163.9{C_{ci}}^{1.00}$, $\beta_{sn} = 10.4{C_{sn}}^{0.78}$, where β is the extinction coefficient for each water species, which is associated with the mass concentration (g m^{-3}) of cloud liquid water C_{cw}, rain water C_{rw}, cloud ice C_{ci}, and snow C_{sn}.	Stoelinga and Warner (1999)
FSL	$\mathrm{VIS_{FSL}} = 1.609 \times 6000 \times (T - T_d)/\mathrm{rh}^{1.75}$, where rh is the relative humidity and $T - T_d$ is the dew point depression (°C).	Doran et al. (1999)
CVIS	$\mathrm{VIS_{CVIS}} = \min(\mathrm{VIS_{SW99}}, \mathrm{VIS_{FSL}})$.	Bang et al. (2009)
AFWA	$\mathrm{VIS_{AFWA}} = \min(\mathrm{VIS_{hydro}}, \mathrm{VIS_{dust}}, \mathrm{VIS_{fog}})$. AFWA visibility diagnostics takes the minimum of the visibility due to hydrometeors, dust, and fog/haze.	Creighton et al. (2014)
	Visibility due to hydrometers: $\mathrm{VIS_{hydro}} = -\ln(0.02)/\beta_{hydro}$, $\beta_{hydro} = \left(1.1 \times (C_{rw} + C_{gp})^{0.75} + 10.36{C_{sn}}^{0.78}\right)/1000$, where C_{rw}, C_{gp}, and C_{sn} are the mass concentrations in g m^{-3} for rain water, graupel, and snow, respectively.	
	Visibility due to dust obscuration: $\mathrm{VIS_{dust}} = -\ln(0.02)/\beta_{dust}$, $\beta_{dust} = \sum_{i=1}^{5} 1.5 \times C_i/(\rho_i \times r_{eff,i})$, where C_i is the mass concentration, ρ_i is the density, and $r_{eff,i}$ is the effective radius of dust bin i.	
	Visibility due to fog/haze: $\mathrm{VIS_{fog}} = 1500 \times (105 - \mathrm{rh2}) \times (5/\mathrm{mix2})$, where rh2 is the 2-m relative humidity and mix2 is the 2-m mixing ratio.	
UPP1	$\mathrm{VIS_{UPP1}} = \min(24.135, -\ln(0.02)/\beta)$, $\beta = \beta_{cw} + \beta_{rw} + \beta_{ci} + \beta_{sn}$, $\beta_{cw} = 144.7{C_{cw}}^{0.88}$, $\beta_{rw} = 2.24{C_{rw}}^{0.75}$, $\beta_{ci} = 327.8{C_{ci}}^{1.00}$, $\beta_{sn} = 10.36{C_{sn}}^{0.7776}$. This algorithm, used in NCEP Unified Post Processor versions 2.2 (UPP2.2), follows SW99, with some minor modifications of the constants.	UPP2.2
GSD	$\mathrm{VIS_{GSD}} = \min(\mathrm{VIS_{rh}}, \mathrm{VIS_{hydro}})$. This algorithm, used in NCEP Unified Post Processor versions 2.2 (UPP2.2), takes the minimum of the visibility due to relative humidity and hydrometeors.	UPP2.2
	$\mathrm{VIS_{rh}} = 60.0 \times \exp(-2.5 \times q_{rh})$, $q_{rh} = \min(0.8, (\mathrm{rh_{max}}/100 - 0.15))$, where $\mathrm{rh_{max}}$ is the maximum relative humidity at the lowest two model levels. The inhibition of low-level wind shear to reduced visibility can also be considered.	
	$\mathrm{VIS_{hydro}} = \min(90.0, -\ln(0.02)/\beta + \beta_0)$, $\beta = \beta_{cw} + \beta_{rw} + \beta_{ci} + \beta_{sn} + \beta_{gp} + 1.E-10$, $\beta_{cw} = 144.7{C_{cw}}^{0.88}$, $\beta_{rw} = 2.24{C_{rw}}^{0.75}$, $\beta_{ci} = 327.8{C_{ci}}^{1.00}$, $\beta_{sn} = \alpha_{sn} \times {C_{sn}}^{1.00}$, $\beta_{gp} = 4.0{C_{gp}}^{0.75}$. $\mathrm{VIS_{hydro}}$ mainly follows $\mathrm{VIS_{UPP1}}$, with the addition of extinction coefficients for graupel C_{gp} and aerosol β_0, and the extinction coefficient for snow C_{sn}, varying with the temperature α_{sn}. It can also consider the impact of night and day on the visibility.	
G2006	$\mathrm{VIS_{G2006}} = 1.002/(\mathrm{LWC} \times N_d)^{0.6473}$, $N_d = -0.071T^2 + 2.213T + 141.56$.	Gultepe et al. (2006)
G2009	$\mathrm{VIS_{G2009}} = 0.87706/(\mathrm{LWC} \times N_d)^{0.49034}$, $N_d = -0.071T^2 + 2.213T + 141.56$.	Gultepe et al. (2009)

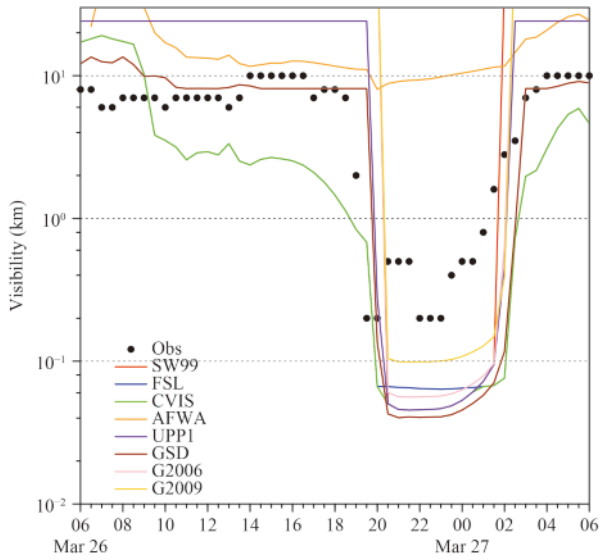

Fig. 5. Time series of WRF-simulated visibility at ZSPD from different algorithms (colored curves), compared with the Meteorological Aviation Report (METAR) data (black dots) from 0600 UTC 26 to 0600 UTC 27 March 2014. Note that the visibility values above 10 km are considered unlimited in the METAR reports. The figure uses a logarithmic scale on the *y* axis, so the actual differences between various schemes and observations are small.

tems at the Meteorological Center of East China ATMB, are selected and examined.

4.1 *Forecast lead time*

Initial conditions are vital for accurate NWP. In order to identify the impact of initial conditions on forecast results with different forecast lead times, and also to select an initial time that allows for fair comparison of the sensitivity experiments with various physical parameterization schemes, we first evaluate the impact of forecast lead times on the numerical forecasts of the fog event.

Experiments with four different forecast lead times are conducted for the fog event. They are designed as a 36-h forecast initiated at 1800 UTC 25 March (Mar2518, hereafter), a 30-h forecast initiated at 0000 UTC 26 March (Mar2600), a 24-h forecast initiated at 0600 UTC 26 March (Mar2606), and an 18-h forecast initiated at 1200 UTC 26 March (Mar2612), with forecast lead times (relative to the fog onset at around 19 UTC 26 March) of 25, 19, 13, and 7 h, respectively.

Figure 6a compares the observed and simulated visibilities at ZSPD. Apparently, the simulations by Mar2600 and Mar2606 produce similar and accurate timing of the fog onset. Simulations by Mar2518 and Mar2600 have generated almost the same and the latest dispersal (3.5 h later than observation), while Mar2612 predicts the earliest dispersal. Meanwhile, a 12-h simulation initiated at 1800 UTC 26 March is also conducted. Since it is not able to capture the fog event even with the best initial conditions (the shortest forecast lead time with conditions similar to the FNL analysis, and SYNOP and METAR observations), the details of the results from this experiment are not shown. Considering the timing of both the onset and dispersal of this fog event, the simulation Mar2606 (initiated at 0600 UTC 26 March with a forecast lead time of 13 h) gives the best performance and captures the closest onset and dispersal time. Similar results of better forecasting with longer forecast lead times were also presented by Radi et al. (2008) and Román-Cascón et al. (2016), but for different areas or different fog types. Radi et al. (2008) found that coastal fog occurrence in the UAE was well predicted with a forecast lead time of 24 h or more when GFS analysis was used as initial states, while Román-Cascón et al. (2016) concluded that simulations with a forecast lead

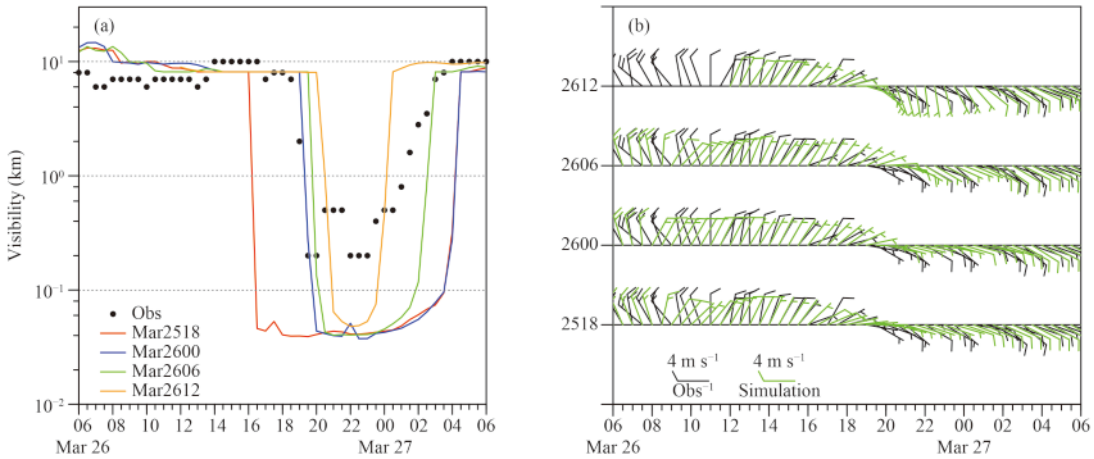

Fig. 6. (a) As in Fig. 5, but for simulations with different forecast lead times at 1800 UTC 25, 0000 UTC 26, 0600 UTC 26, and 1200 UTC 26 March 2014. (b) Time series of simulated winds at 10 m from different forecast lead times, compared against the observations at ZSPD.

time of 30 h were usually better than those with only 6 h of spin-up time, based on their radiation fog cases in Spain and the Netherlands.

The reason that a shorter lead time does not lead to a better forecast lies in the inadequacy of the spin-up and the physical quantities required to reproduce the physical variables in the forecasts, especially those (e.g., liquid water content) related to the visibility calculation. This can be proved by further examining the atmospheric conditions reproduced by the different simulation experiments. A comparison of the simulated surface synoptic situation with SYNOP surface observations (figures omitted) and the time series of winds at 10 m with METAR at ZSPD (Fig. 6b) is conducted. Experiment Mar2612 does not have enough time to reproduce the cold trough at the lower levels near the surface over the western ECS, leading to the inability of the model to provide efficient cooling of the lower levels, and thus producing no high values of RH over the sea. As a result, no fog is simulated over the sea near the coastal area and no fog is advected to ZSPD from the sea. Instead, the simulated fog by Mar2612 forms inland with a shorter duration at ZSPD. For Mar2618, there is even no time for the model to spin up (trigger) related physical processes to produce high values of RH and fog, since the fog "wall" arrived at ZSPD at 1930 UTC, which is just 1.5 h apart from the initial time. In contrast, results from Mar2518, Mar2600, and Mar2606 indicate that the synoptic situations are more or less similar for different initial times, with a slightly better simulation for relatively shorter forecast lead times. These simulations have had enough time to develop the associated physical processes, and successfully captured the fog over the sea before it advected to ZSPD. Among these experiments, Mar2518 produces the largest area of fog distribution, along with Mar2600. The simulated easterlies at the lower levels around the ZSPD region by Mar2518 and Mar2600 persist longer than that by Mar2606, resulting in later dissipation of the fog at ZSPD and indicating the importance of the wind direction in the formation and duration of advection fog at ZSPD.

4.2 *Microphysics schemes*

Microphysical parameterization (MP) schemes allow NWP models to depict cloud processes that occur at the micro scale and cannot be properly resolved, which is important for fog formation and evolution. Previous studies (Radi et al., 2008; Tudor, 2010; Van der Velde et al., 2010; Steeneveld et al., 2015) have investigated MP impacts on various fog episodes, especially on radiation fog, and showed varying sensitivities of MP on different fog cases. In this study, several MP schemes available in the WRF model are employed to investigate the sensitivity of the aforementioned advection fog event to the choices of MP schemes, with the other settings (all other physical schemes and domain configurations) being kept the same as in the control simulation mentioned in Section 3. We only consider the MP schemes that have been heavily tested at the Meteorological Center of East China ATMB, so the Thompson (Thompson et al., 2008), WRF single-moment six class scheme (WSM6) (Hong and Lim, 2006), WRF double-moment six class scheme (WDM6) (Lim and Hong, 2010), and Morrison double-moment (Morrison et al., 2009) scheme are chosen in the simulations. Other physical schemes are also compared and show similar results (figures omitted).

The simulated visibilities (Fig. 7) show that the four MP schemes predict the fog event with similar timing of fog onset but large discrepancies in fog dispersal. The simulation with the WDM6 scheme predicts the longest duration with the latest fog dispersal at ZSPD and the lowest visibility, while the simulation with the Thompson scheme predicts fog duration comparable with the observations. The other two schemes also predict fog dispersal more than 1 h later. Note that the timing of fog dissipation coincides with the time when the simulated dew point depression $T - T_d$ increases or RH decreases rapidly. Thus, the better simulation of the variation of $T - T_d$ and RH leads to a better simulation of the timing of fog dissipation at ZSPD (figures omitted).

To further examine the reasons for the difference in visibility forecasts with the various MP schemes, the

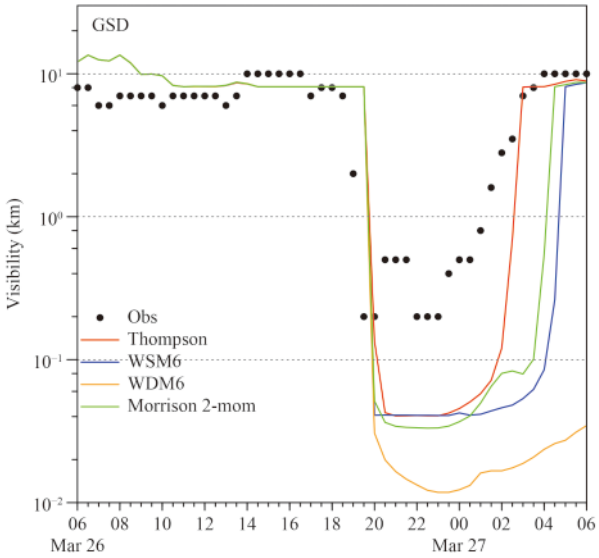

Fig. 7. As in Fig. 5, but for the experiments with different microphysical schemes.

simulated cloud water mixing ratio (q_c; g kg^{-1}) at the lowest model level (figure omitted) and its vertical distribution (Fig. 8) at ZSPD, as well as the horizontal distribution of q_c at the lowest model level and the vertically integrated cloud water content (figure omitted), are all compared. A substantial sensitivity of these variables to the MP schemes is found, along with different times of fog dissipation and maximum q_c values within the fog's lifetime. Specifically, the maximum q_c at the lowest model level at ZSPD during the fog period varies from 0.45 g kg^{-1} (Thompson) to more than 1.9 g kg^{-1} (WDM6).

It is also noted that the simulated q_c and visibility are quite similar in the three single-moment schemes (WSM3, WSM5, and WSM6) of the WRF model, and the two double-moment schemes (WDM5 and WDM6), respectively. The reason for these similarities could be that the selected event is a warm fog case without precipitation, in which liquid water (cloud water) dominates over the condensed water species. This could not manifest the difference between the three WSM schemes or the two WDM schemes by considering a greater or lesser number of hydrometeors (ice, snow, and graupel) and whether to allow mixed phases and ice, snow, and graupel processes. In addition, the WDM schemes predict much higher liquid water content than the WSM schemes, which is similar to the results of Steeneveld et al. (2015).

It seems that the simulation of fog dissipation is more sensitive to MP schemes, which agrees with the result of Steeneveld et al. (2015) that the fog dispersal is associated more with the microphysical processes.

4.3 *PBL schemes*

The PBL is the lowest part of the atmosphere where physical quantities display strong turbulence and vertical mixing, and it plays an important role in fog formation and evolution. The sensitivity of fog simulation to the three widely used options of the YSU (Hong et al., 2006), MYJ (Janjić, 1994), and ACM2 (Asymmetric Convective Model version 2; Pleim, 2007) schemes is investigated. Other physical settings are the same as those

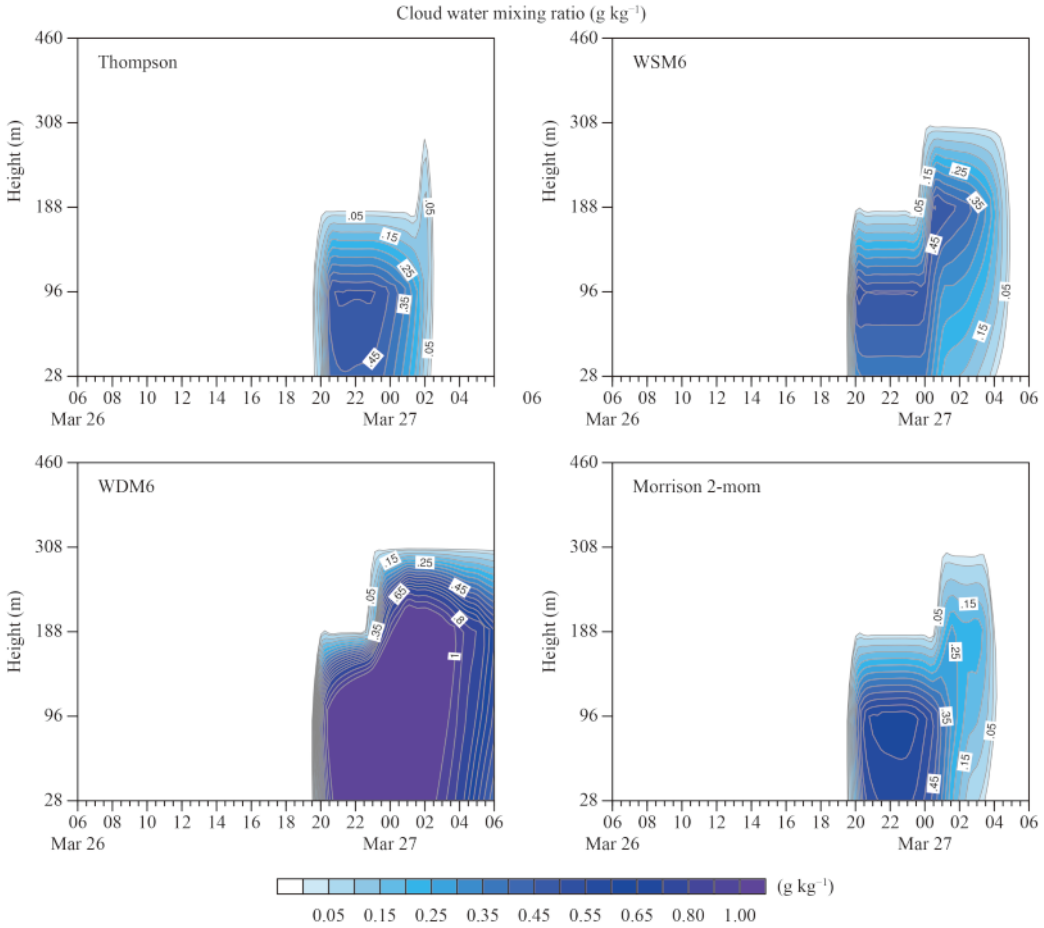

Fig. 8. Temporal variations of the cloud water mixing ratio q_c (g kg^{-1}) with height at ZSPD from 0600 UTC 26 to 0600 UTC 27 March 2014, from the simulations using different microphysical schemes.

used in the control run, except that the surface-layer option is set to the Monin–Obukhov scheme (Eta similarity) when the MYJ scheme is used. Specifically, the YSU and ACM2 are first-order closure schemes, while the MYJ is a turbulent kinetic energy closure scheme.

Figure 9 shows that the fog prediction (e.g., visibility) is sensitive to various PBL schemes. The time series of the vertical distribution of q_c at ZSPD from the experiments using different PBL schemes was compared. It is found that the MYJ scheme predicts the shortest duration of fog at ZSPD, which corresponds to the shortest fog persistence and a later onset and earlier dispersal than observed, as shown in Fig. 9. The YSU and ACM2 schemes generate relatively accurate and longer duration of cloud water that extends to the lowest model level, corresponding to an accurate visibility calculation. In addition, with three surface-layer options, the simulation with the ACM2 scheme successfully predicts the process of fog uplifting into low clouds, while the simulation with the YSU scheme using the old MM5 surface-layer process predicts a short time uplifting of fog into low clouds (figures omitted); and in general, the simulated q_c by the different surface layer schemes does not show obvious differences.

Figure 10 shows the horizontal distribution of q_c at the lowest model level and the satellite visible images from MTSAT (Multifunctional Transport Satellites). The satellite images show that the fog covers the sea along the coastal area around the ZSPD region. With the YSU and ACM2 schemes, a large area of horizontal q_c is distributed over the sea, while the simulation with the MYJ scheme fails to simulate the fog over the related area. Between the YSU and ACM2 schemes, the simulated q_c by the ACM2 scheme extends to a larger area than that of the YSU scheme. Meanwhile, the temporal variation of the horizontal distribution of q_c at the lowest model level shows that, with the MYJ scheme, the simulated fog at ZSPD forms locally rather than moving from the ECS (figures omitted).

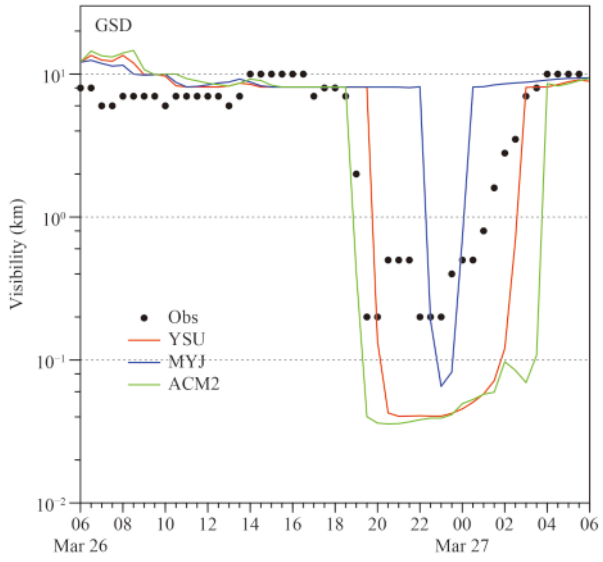

Fig. 9. As in Fig. 5, but for the experiments with different PBL schemes.

Further comparison is conducted for winds at 10 m, and T and T_d at 2 m. Figure 11 shows that these variables are sensitive to the PBL schemes as soon as the simulation starts. In the simulations with the YSU and ACM2 schemes, the winds are comparable with the observations in both speed and direction during the fog event and at its dissipation. The overall trend of the temporal variation of T and T_d exhibits a decline, but there is a sharp increase (peak) when the fog approaches ZSPD, corresponding to the time when the calculated visibility is less than 1 km. This is due to the "wall" of the fog with warmer and moister air moving from the sea to ZSPD, where it was originally dominated by relatively cooler and drier air, leading to the sudden increase of T and T_d. The simulation with the MYJ scheme reproduces more wind veering to the southeast and a lower wind speed (< 2 m s^{-1}) during the fog event, compared with the other two schemes and observations. With the MYJ scheme, T and T_d decrease gradually to their minimums before the fog onset, persist during the fog maintenance, and increase sharply from being underestimated to being overestimated during the fog's dissipation. This may explain why the simulated fog forms locally and does not advect from the ECS, making it much more like a radiation fog event. Overall, YSU and ACM2 perform better than the MYJ PBL scheme in this case.

4.4 *Longwave radiation*

To evaluate the impact of longwave radiation (RALW) schemes on fog and visibility simulation with WRF, experiments with the RRTM (Mlawer et al., 1997), RRTMG (Iacono et al., 2008), and GFDL (Fels and Schwarzkopf, 1981) longwave radiation schemes are employed together with the YSU and ACM2 PBL schemes, while the other model settings are based on the control run configuration, in which RRTMG is used in the simulation.

The vertical distribution of q_c at ZSPD with RALW schemes based on the Thompson–YSU and Thompson–ACM2 schemes is shown in Fig. 12. The temporal variation of the vertical q_c shows that the simulated fog and visibility are also sensitive to the RALW schemes during both fog onset and dispersal. Except for the combination of GFDL with Thompson–YSU, the simulated maximum

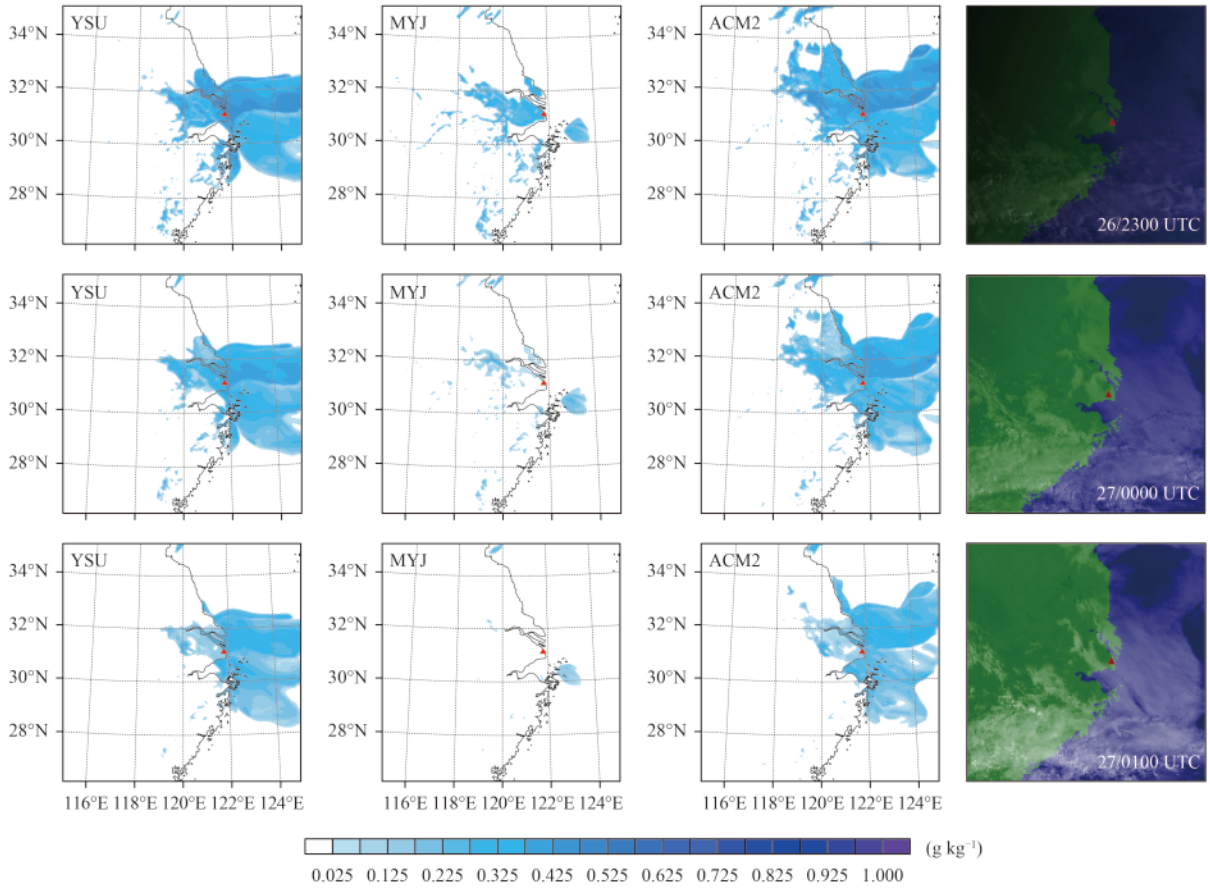

Fig. 10. Horizontal distributions of cloud liquid water (q_c; g kg^{-1}) at the lowest model level from the simulations with the YSU (left most column), MYJ (second column from left), and ACM2 (third from left) PBL schemes, and visible images (right most column) from MTSAT (Multifunctional Transport Satellites), at 2300 UTC 26 (top panels), 0000 UTC 27 (middle panels), and 0100 UTC 27 March 2014 (bottom panels).

q_c values at the lowest model level at ZSPD are comparable among the simulations with various RALW schemes. The horizontal distribution of simulated cloud water with the RRTM scheme using the Thompson + YSU (Thompson + ACM2) scheme shows that the fog forms earliest, at about 0900 UTC 26 March (0800 UTC 26 March), and extends to a larger area over the ECS region northeast of ZSPD, than that with the RRTMG scheme, which results in the earliest fog onset and latest fog dispersal at ZSPD among the selected RALW schemes with both PBL schemes. The simulation by the GFDL scheme shows the shortest fog duration with the Thompson + YSU scheme but performs comparably to the other schemes using the Thompson + ACM2 scheme. The results show that the simulation with the GFDL scheme is sensitive to the PBL scheme used. Differences in the simulations with the GFDL scheme depend on the extension of fog itself simulated by different PBL schemes. For a relatively small extension of fog, as with the YSU scheme (upper right panel in Fig. 12), the GFDL scheme simulates an even smaller extension of fog over the sea that reaches ZSPD for a very short period; whereas for a larger extension of fog in the simulation with ACM2, the GFDL scheme can simulate a comparable fog extension over the sea and fog duration at ZSPD.

The simulated T, T_d, $T - T_d$, and RH at 2 m, and the winds at 10 m, are similar for the first 3 h of forecast, and then gradually vary with different RALW schemes. The wind directions are quite similar (i.e., not sensitive to RALW schemes) and correspond well with the observations, except with earlier veering.

4.5 *Shortwave radiation*

Three shortwave radiation (RASW) schemes in WRF: Dudhia (Dudhia, 1989), RRTMG (Iacono et al., 2008), and FLG (Fu and Liou, 1992; Gu et al., 2011), are evaluated. Among these schemes, Dudhia is used in the control run. Results are shown for the experiments designed with Thompson (MP) + YSU (PBL) + RRTMG (RALW) and Thompson (MP) + ACM2 (PBL) + RRTMG

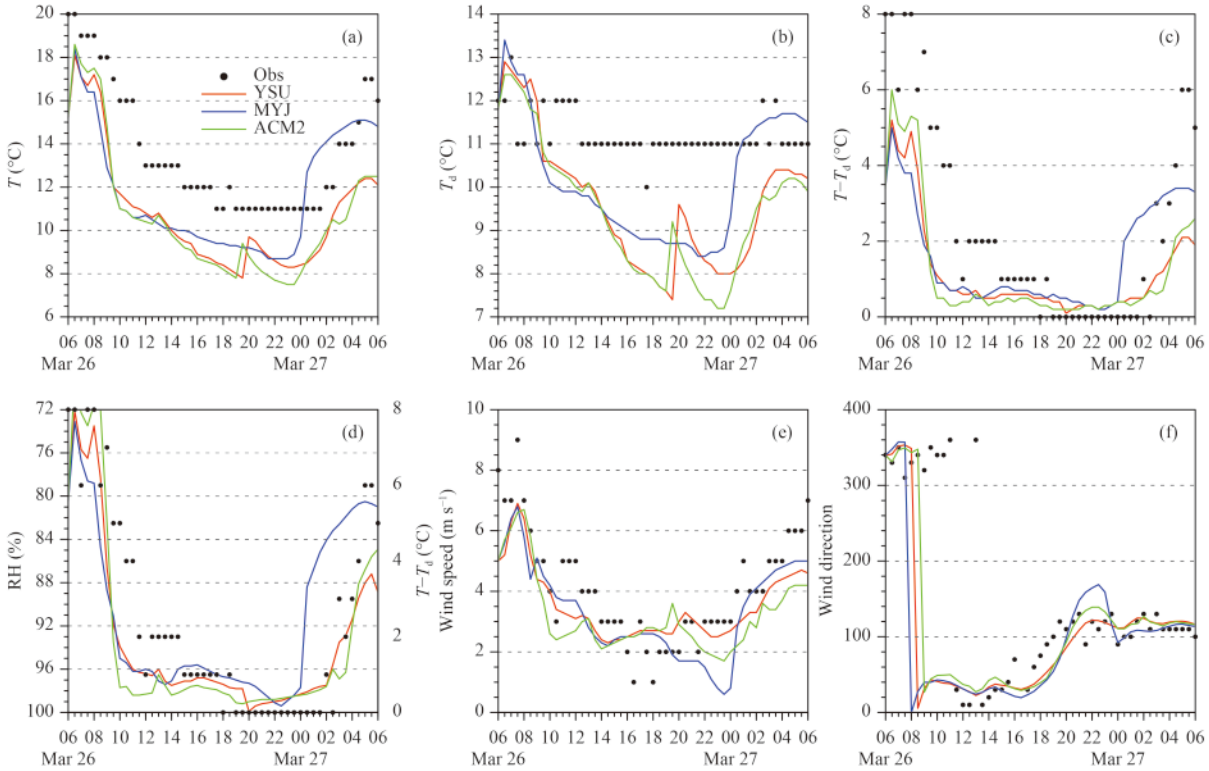

Fig. 11. Comparison between the observed and simulated (a) temperature (T), (b) dew point temperature (T_d), (c) dew point depression ($T - T_d$), (d) RH, (e) wind direction, and (f) wind speed with different PBL schemes at ZSPD during the simulation period.

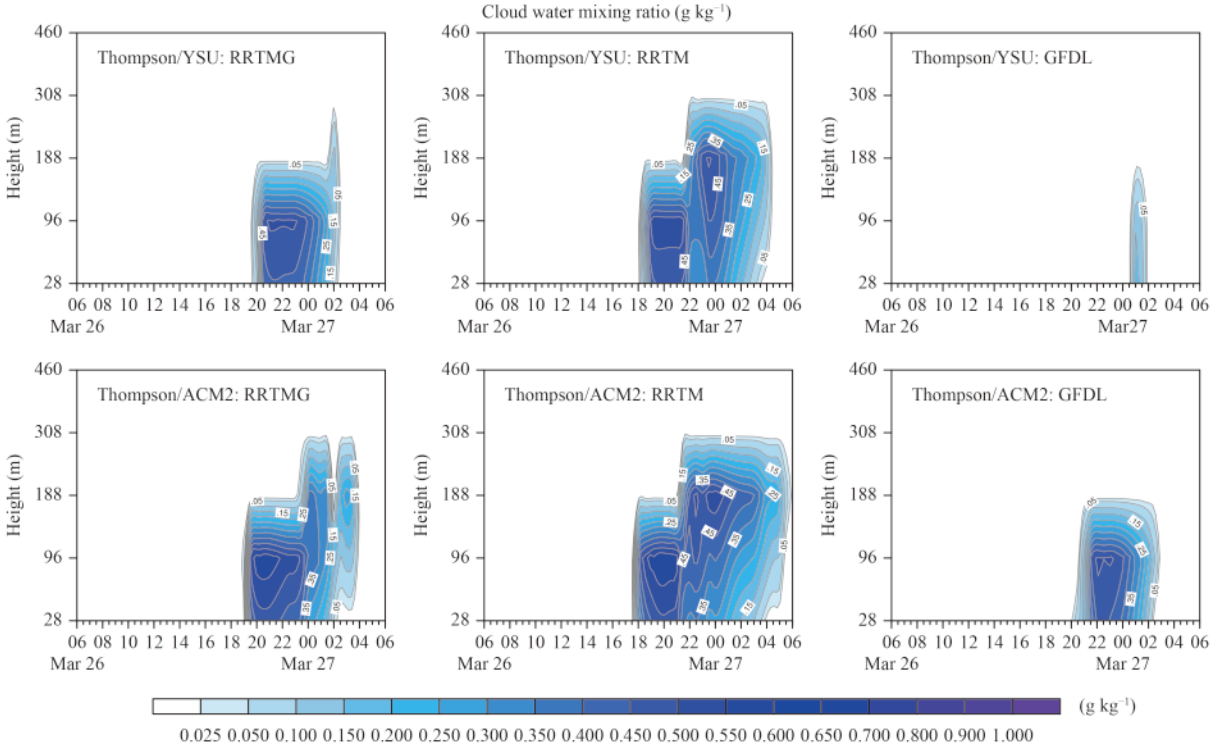

Fig. 12. As in Fig. 8, but for the experiments with different longwave radiation schemes in combination with two PBL schemes.

(RALW), with the other model settings based on the control run configuration.

The synoptic conditions and the average RMSE of the simulated T, T_d, and $T - T_d$ at 2 m, the winds at 10 m, and

SLP from 0900 UTC 26 March to 0600 UTC 27, are first compared. Two FLG RASW schemes with YSU and ACM2 PBL schemes predict much larger RMSEs in T, T_d, and $T - T_d$ at 2 m, and in SLP, than the other schemes, with notable differences during fog dissipation (figures omitted).

Regardless of the FLG scheme, the vertical distributions of q_c and the calculated visibilities (Fig. 13) show that they are slightly sensitive to the RASW scheme, perhaps due to the fact that the fog developed and persisted during the night [0130–0930 BJT (Beijing time) 27 March]. For the FLG scheme, there is no simulated downward shortwave flux at the ground surface (all equal to 0), which results in fog persistence for the remainder of the model run, even when the sun rises.

5. Summary and concluding remarks

This paper aims to investigate the sensitivity of numerical simulations of an advection fog event to forecast lead times and the parameterization schemes of physical processes, such as microphyics, PBL, longwave and shortwave radiation, with the main focus on visibility and fog simulation at ZSPD. A case with typical synoptic conditions of an advection fog during 26–27 March 2014 is selected and examined by using the WRF model.

The sensitivity to the initial times shows that selection of an appropriate forecast lead time is important for providing relatively good initial conditions and allowing enough spin-up of the model and completion of the physical processes. The simulation with a short forecast lead time cannot reproduce the fog event due to insufficient time for the model spin-up of physical processes to provide efficient cooling at the lower levels for fog formation, though it can provide better large-scale initial conditions. For the studied case, the simulations with a forecast lead time of more than 12 h are able to predict the fog over the ECS and then the fog advection to ZSPD, though different forecast lead times lead to different fog onset times and areal extensions, with larger extension leading to longer fog duration. The results suggest a trade-off between more accurate initial conditions and a proper forecast lead time that allows for model physical processes to spin up adequately.

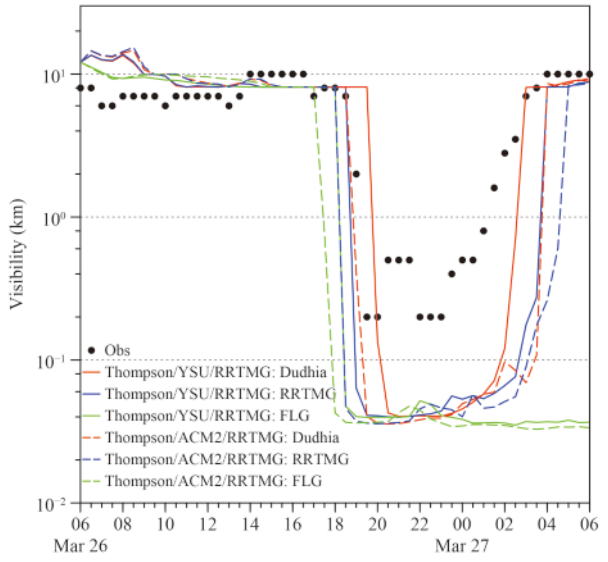

Fig. 13. As in Fig. 5, but for the experiments with different RASW schemes and PBL schemes.

Sensitivity experiments with different microphysical parameterization schemes indicate that the simulated fog dissipation, instead of fog onset, is associated more with the microphysical parameterization scheme, implying that microphysical parameterization is not a determining factor for fog formation. This agrees with the result reported by Steeneveld et al. (2015) that fog dissipation is more sensitive to the microphysical schemes.

A substantial sensitivity of the fog onset and dissipation to the PBL scheme is also confirmed. Specifically, the MYJ scheme fails to predict the fog over the sea and its advection to ZSPD but predicts a short duration of fog locally with the latest fog onset and earliest fog dispersal; whereas the simulations with YSU and ACM2 are comparable with the observations, with larger extension of fog simulated by ACM2. The simulation with ACM2 also predicts the process of fog uplifting into low clouds, as reported by METAR. The combination of different surface layer options with the YSU and ACM2 PBL schemes does not show a markedly different impact on the fog simulation.

The simulation of fog onset and dissipation is also sensitive to longwave and shortwave radiation schemes. Most schemes can capture the fog event but with different timings of fog onset and dispersal. For the longwave radiation schemes, the results indicate that the simulation by the GFDL scheme is highly sensitive to the extension of the fog simulated by the permutated PBL scheme, with a relatively small extension of fog simulation permutated with the YSU PBL scheme leading to an even smaller extension of fog over the sea that reaches ZSPD for a very short period. For the longwave radiation schemes, the FLG scheme fails to predict fog dissipation due to a lack of modeled downward shortwave flux at the ground.

Although this study focuses on ZSPD, the conclusions are almost the same for simulations at two other

nearby coastal airports (Nantong and Zhoushan; results not shown in this paper), where advection fog is also observed. In addition, despite the fact that most of the conclusions from this study are based on only one case without statistical robustness, the overall results imply that appropriate forecast lead times and physical parameterization schemes employed in an NWP model are critical to the successful prediction of a fog event. The uncertainty in model initial conditions and model physical parameterizations could play an essential role in the numerical prediction of fog. This suggests that ensemble forecasting (e.g., Zhou and Du, 2010) and data assimilation may be good methods for improving fog forecasting. Future studies will attempt to analyze more cases of various fog types with improved model parameterizations, through approaches of ensemble forecasting and/or data assimilation as priority considerations.

REFERENCES

Bang, C. H., J. W. Lee, and S. Y. Hong, 2009: Predictability experiments of fog and visibility in local airports over Korea using the WRF model. *J. Korean Soc. Atmos. Environ.*, **24**, 92–101.

Bari, D., T. Bergot, and M. El Khlifi, 2015: Numerical study of a coastal fog event over Casablanca, Morocco. *Quart. J. Roy. Meteor. Soc.*, **141**, 1894–1905, doi: 10.1002/qj.2494.

Bergot, T., and D. Guedalia, 1994: Numerical forecasting of radiation fog. Part I: Numerical model and sensitivity tests. *Mon. Wea. Rev.*, **122**, 1218–1230, doi: 10.1175/1520-0493(1994)122<1218:NFORFP>2.0.CO;2.

Bergot, T., E. Terradellas, J. Cuxart, et al., 2007: Intercomparison of single-column numerical models for the prediction of radiation fog. *J. Appl. Meteor. Climatol.*, **46**, 504–521, doi: 10.1175/JAM2475.1.

Bieringer, P. E., M. Donovan, F. Robasky, et al., 2006: A characterization of NWP ceiling and visibility forecasts for the terminal airspace. Preprints, 12th Conference on Aviation Range and Aerospace Meteorology, Atlanta, GA, Amer. Meteor. Soc., 3 pp. [Accessed 10 July 2017 at http://ams. confex.com/ams/Annual2006/techprogram/paper_103720.htm].

Bott, A., and T. Trautmann, 2002: PAFOG—A new efficient forecast model of radiation fog and low-level stratiform clouds. *Atmos. Res.*, **64**, 191–203, doi: 10.1016/S0169-8095(02)00091-1.

Chen, F., and J. Dudhia, 2001: Coupling an advanced land surface–hydrology model with the Penn State–NCAR MM5 modeling system. Part I: Model implementation and sensitivity. *Mon. Wea. Rev.*, **129**, 569–585, doi: 10.1175/1520-0493(2001)129<0569:CAALSH>2.0.CO;2.

Clark, P. A., and W. P. Hopwood, 2001a: One-dimensional site-specific forecasting of radiation fog. Part I: Model formulation and idealized sensitivity studies. *Meteor. Appl.*, **8**, 279–286, doi: 10.1017/S1350482701003036.

Clark, P. A., and W. P. Hopwood, 2001b: One-dimensional site-specific forecasting of radiation fog. Part II: Impact of site observations. *Meteor. Appl.*, **8**, 287–296.

Creighton, G., E. Kuchera, R. Adams-Selin, et al., 2014: AFWA Diagnostics in WRF. [Accessed 10 July 2017 at http://www2.mmm.ucar.edu/wrf/users/docs/AFWA_Diagnostics_in_WRF.pdf].

Doran, J. A., P. J. Roohr, D. J. Beberwyk, et al., 1999: The MM5 at the Air Force Weather Agency—New products to support military operations. The 8th Conference on Aviation, Range, and Aerospace Meteorology, NOAA/NWS, Dallas, Texas.

Dudhia, J., 1989: Numerical study of convection observed during the Winter Monsoon Experiment using a mesoscale two-dimensional model. *J. Atmos. Sci.*, **46**, 3077–3107, doi: 10.1175/1520-0469(1989)046<3077:NSOCOD>2.0.CO;2.

Fabbian, D., R. de Dear, and S. Lellyett, 2007: Application of artificial neural network forecasts to predict fog at Canberra International Airport. *Wea. Forecasting*, **22**, 372–381, doi: 10.1175/WAF980.1.

Fels, S. B., and M. D. Schwarzkopf, 1981: An efficient, accurate al-gorithm for calculating CO_2 15 μm band cooling rates. *J. Geo-phys. Res.*, **86**, 1205–1232, doi: 10.1029/JC086iC02p01205.

Fu, Q., and K. N. Liou, 1992: On the correlated *k*-distribution method for radiative transfer in nonhomogeneous atmospheres. *J. Atmos. Sci.*, **49**, 2139–2156, doi: 10.1175/1520-0469(1992)049<2139:OTCDMF>2.0.CO;2.

Fu, G., P. Y. Li, J. G. Crompton, et al., 2010: An observational and modeling study of a sea fog event over the Yellow Sea on 1 August 2003. *Meteor. Atmos. Phys.*, **107**, 149–159, doi: 10.1007/s00703-010-0073-0.

Golding, B. W., 1993: A study of the influence of terrain on fog development. *Mon. Wea. Rev.*, **121**, 2529–2541, doi: 10.1175/1520-0493(1993)121<2529:ASOTIO>2.0.CO;2.

Gu, Y., K. N. Liou, S. C. Ou, et al., 2011: Cirrus cloud simulations using WRF with improved radiation parameterization and increased vertical resolution. *J. Geophys. Res.*, **116**, D06119, doi: 10.1029/2010JD014574.

Gultepe, I., and J. A. Milbrandt, 2010: Probabilistic parameterizations of visibility using observations of rain precipitation rate, relative humidity, and visibility. *J. Appl. Meteor. Climatol.*, **49**, 36–46, doi: 10.1175/2009JAMC1927.1.

Gultepe, I., M. D. Müller, and Z. Boybeyi, 2006: A new visibility parameterization for warm-fog applications in numerical weather prediction models. *J. Appl. Meteor.*, **45**, 1469–1480, doi: 10.1175/JAM2423.1.

Gultepe, I., R. Tardif, S. C. Michaelides, et al., 2007: Fog research: A review of past achievements and future perspectives. *Pure Appl. Geophys.*, **164**, 1121–1159, doi: 10.1007/s00024-007-0211-x.

Gultepe, I., B. Hansen, S. G. Cober, et al., 2009: The fog remote sensing and modeling field project. *Bull. Amer. Meteor. Soc.*, **90**, 341–359, doi: 10.1175/2008BAMS2354.1.

Gultepe, I., B. Zhou, J. Milbrandt, et al., 2015: A review on ice fog measurements and modeling. *Atmos. Res.*, **151**, 2–19, doi: 10.1016/j.atmosres.2014.04.014.

Hong, S. Y., and J. O. J. Lim, 2006: The WRF single-moment 6-class microphysics scheme (WSM6). *J. Korean Meteor. Soc.*, **42**, 129–151.

Hong, S. Y., Y. Noh, and J. Dudhia, 2006: A new vertical diffusion package with an explicit treatment of entrainment pro-

cesses. *Mon. Wea. Rev.*, **134**, 2318–2341, doi: 10.1175/ MWR 3199.1.

Hu, H. Q., Q. H. Zhang, B. G. Xie, et al., 2014: Predictability of an advection fog event over North China. Part I: Sensitivity to initial condition differences. *Mon. Wea. Rev.*, **142**, 1803–1822, doi: 10.1175/MWR-D-13-00004.1.

Iacono, M. J., J. S. Delamere, E. J. Mlawer, et al., 2008: Radiative forcing by long-lived greenhouse gases: Calculations with the AER radiative transfer models. *J. Geophys. Res.*, **113**, doi: 10.1029/2008JD009944.

Janjić, Z. I., 1994: The step-mountain eta coordinate model: Further developments of the convection, viscous sublayer, and turbulence closure schemes. *Mon. Wea. Rev.*, **122**, 927–945, doi:10.1175/1520-0493(1994)122<0927:TSMECM>2.0.CO;2.

Kain, J. S., 2004: The Kain–Fritsch convective parameterization: An update. *J. Appl. Meteor.*, **43**, 170–181, doi: 10.1175/1520-0450(2004)043<0170:TKCPAU>2.0.CO;2.

Kim, C. K., and S. S. Yum, 2012: A numerical study of sea-fog formation over cold sea surface using a one-dimensional turbulence model coupled with the Weather Research and Forecasting Model. *Bound.-Layer Meteor.*, **143**, 481–505, doi: 10.1007/s10546-012-9706-9.

Li, Y. P., and Y. X. Zheng, 2015: Analysis of atmospheric turbulence in the upper layers of sea fog. *Chinese J. Oceanol. Limnol.*, **33**, 809–818, doi: 10.1007/s00343-015-4030-0.

Lim, K. S. S., and S. Y. Hong, 2010: Development of an effective double-moment cloud microphysics scheme with prognostic cloud condensation nuclei (CCN) for weather and climate models. *Mon. Wea. Rev.*, **138**, 1587–1612, doi: 10.1175/2009 MWR2968.1.

Lin, Y. L., R. D. Farley, and H. D. Orville, 1983: Bulk parameterization of the snow field in a cloud model. *J. Climate Appl. Meteor.*, **22**, 1065–1092, doi: 10.1175/1520-0450(1983)022 <1065:BPOTSF>2.0.CO;2.

Mlawer, E. J., S. J. Taubman, P. D. Brown, et al., 1997: Radiative transfer for inhomogeneous atmospheres: RRTM, a validated correlated-k model for the longwave. *J. Geophys. Res.*, **102**, doi: 10.1029/97JD00237.

Morrison, H., G. Thompson, and V. Tatarskii, 2009: Impact of cloud microphysics on the development of trailing stratiform precipitation in a simulated squall line: Comparison of one- and two-moment schemes. *Mon. Wea. Rev.*, **137**, 991–1007, doi: 10.1175/2008MWR2556.1.

Nakanishi, M., and H. Niino, 2006: An improved Mellor–Yamada level-3 model: Its numerical stability and application to a regional prediction of advection fog. *Bound.-Layer Meteor.*, **119**, 397–407, doi: 10.1007/s10546-005-9030-8.

Niu, S. J., C. S. Lu, H. Y. Yu, et al., 2010: Fog research in China: An overview. *Adv. Atmos. Sci.*, **27**, 639–662, doi: 10.1007/s00376-009-8174-8.

Pagowski, M., I. Gultepe, and P. King, 2004: Analysis and modeling of an extremely dense fog event in southern Ontario. *J. Appl. Meteor.*, **43**, 3–16, doi: 10.1175/1520-0450(2004)043 <0003:AAMOAE>2.0.CO;2.

Payra, S., and M. Mohan, 2014: Multirule based diagnostic approach for the fog predictions using WRF modelling tool. *Adv. Meteor.*, **2014**, 456065, doi: 10.1155/2014/456065.

Pleim, J. E., 2007: A combined local and nonlocal closure model for the atmospheric boundary layer. Part I: Model description and testing. *J. Appl. Meteor. Climatol.*, **46**, 1383–1395, doi: 10.1175/JAM2539.1.

Radi, A., A. A. Al-Katheri, and K. Al-Chergui, 2008: Evaluation of United Arab Emirates WRF two-way nested model on a set of thick coastal fog situations. [Accessed 10 July 2017 at http://www2.mmm.ucar.edu/wrf/users/workshops/WS2008/abstracts/P8-06.pdf].

Rémy, S., O. Pannekoucke, T. Bergot, et al., 2012: Adaptation of a particle filtering method for data assimilation in a 1D numerical model used for fog forecasting. *Quart. J. Roy. Meteor. Soc.*, **138**, 536–551, doi: 10.1002/qj.v138.663.

Román-Cascón, C., C. Yagüe, M. Sastre, et al., 2012: Observations and WRF simulations of fog events at the Spanish Northern Plateau. *Adv. Sci. Res.*, **8**, 11–18, doi: 10.5194/asr-8-11-2012.

Román-Cascón, C., G. J. Steeneveld, C. Yagüe, et al., 2016: Forecasting radiation fog at climatologically contrasting sites: Evaluation of statistical methods and WRF. *Quart. J. Roy. Meteor. Soc.*, **142**, 1048–1063, doi: 10.1002/qj.2016.142.issue-695.

Skamarock, W. C., J. B. Klemp, J. Dudhia, et al., 2008: A Description of the Advanced Research WRF Version 3. NCAR Technical Note, NCAR/TN-475+STR, doi: 10.5065/D68S4MVH.

Steeneveld, G. J., R. J. Ronda, and A. A. M. Holtslag, 2015: The challenge of forecasting the onset and development of radiation fog using mesoscale atmospheric models. *Bound.-Layer Meteor.*, **154**, 265–289, doi: 10.1007/s10546-014-9973-8.

Stoelinga, M. T., and T. T. Warner, 1999: Nonhydrostatic, mesobeta-scale model simulations of cloud ceiling and visibility for an East Coast winter precipitation event. *J. Appl. Meteor.*, **38**, 385–404, doi: 10.1175/1520-0450(1999)038 <0385:NMSMSO>2.0.CO;2.

Stolaki, S., I. Pytharoulis, and T. Karacostas, 2012: A study of fog characteristics using a coupled WRF–COBEL model over Thessaloniki airport, Greece. *Pure Appl. Geophys.*, **169**, 961–981, doi: 10.1007/s00024-011-0393-0.

Tang, Y. M., R. Capon, R. Forbes, et al., 2009: Fog prediction using a very high resolution numerical weather prediction model forced with a single profile. *Meteor. Appl.*, **16**, 129–141, doi: 10.1002/met.v16:2.

Tardif, R., 2007: The impact of vertical resolution in the explicit numerical forecasting of radiation fog: A case study. *Pure Appl. Geophys.*, **164**, 1221–1240, doi: 10.1007/s00024-007-0216-5.

Tardif, R., and R. M. Rasmussen, 2007: Event-based climatology and typology of fog in the New York city region. *J. Appl. Meteor. Climatol.*, **46**, 1141–1168, doi: 10.1175/JAM2516.1.

Thompson, G., P. R. Field, R. M. Rasmussen, et al., 2008: Explicit forecasts of winter precipitation using an improved bulk microphysics scheme. Part II: Implementation of a new snow parameterization. *Mon. Wea. Rev.*, **136**, 5095–5115, doi: 10.1175/2008MWR2387.1.

Tudor, M., 2010: Impact of horizontal diffusion, radiation and cloudiness parameterization schemes on fog forecasting in valleys. *Meteor. Atmos. Phys.*, **108**, 57–70, doi: 10.1007/s00703-010-0084-x.

Van der Velde, I. R., G. J. Steeneveld, B. G. J. W. Schreur, et al., 2010: Modeling and forecasting the onset and duration of severe radiation fog under frost conditions. *Mon. Wea. Rev.*,

138, 4237–4253, doi: 10.1175/2010MWR3427.1.

von Glasow, R., and A. Bott, 1999: Interaction of radiation fog with tall vegetation. *Atmos. Environ.*, **33**, 1333–1346, doi: 10.1016/S1352-2310(98)00372-0.

Yuan, X., and Z. H. Chen, 2013: Statistics and monitoring analysis of advection fog at Shanghai Pudong Airport. *J. Meteor. Sci.*, **33**, 95–101, doi: 10.3969/2012jms.0149. (in Chinese)

Zhou, B. B., 2011: Introduction to A New Fog Diagnostic Scheme. NCEP Office Note 466, 43 pp. [Accessed 10 July 2017 at www.emc.ncep.noaa.gov/officenotes/newernotes/on466.pdf].

Zhou, B. B., and J. Du, 2010: Fog prediction from a multimodel mesoscale ensemble prediction system. *Wea. Forecasting*, **25**, 303–322, doi: 10.1175/2009WAF2222289.1.

Zhou, B. B., J. Du, I. Gultepe, et al., 2012: Forecast of low visibility and fog from NCEP: Current status and efforts. *Pure Appl. Geophys.*, **169**, 895–909, doi: 10.1007/s00024-011-0327-x.

Tech & Copy Editor: Lan YI
Language Editor: Colin SMITH